DOI: 10.1002/ ((please add manuscript number))
Article type: Full Paper

Self-Catalysed Growth of Co, N-co-Doped CNTs on Carbon-Encased CoS_x Surface: A Noble-Metal-Free Bifunctional Oxygen Electrocatalyst for Flexible Solid Zn-Air Batteries

Qian Lu, Jie Yu, Xiaohong Zou, Kaiming Liao,* Peng Tan, Wei Zhou, Meng Ni and Zongping Shao*

Mr. Q. Lu, Mrs. X. Zou, Prof. K. Liao, Prof. W. Zhou, Prof. Z. Shao
State Key Laboratory of Materials-Oriented Chemical Engineering,
College of Chemical Engineering,
Nanjing Tech University, Nanjing 210009, China
E-mail: kaimingliao@njtech.edu.cn; shaozp@njtech.edu.cn

Dr. J. Yu, Dr. P. Tan, Prof. M. Ni
Department of Building and Real Estate,
The Hong Kong Polytechnic University,
Hung Hom, Kowloon, Hong Kong 999077, China

Prof. Z. Shao
Department of Chemical Engineering, Curtin University, Perth, WA 6845, Australia

Keywords: Zn-air battery; oxygen electrode; bifunctional electrocatalyst; self-catalysed growth; synergistic effect.

The self-catalysed growth of nanostructures on material surfaces is one of the most time- and cost-effective ways to design multifunctional catalysts for a wide range of applications. Herein, we reported the use of this technique to develop a multicomponent composite catalyst with CoS_x core encapsulated in ultrathin porous carbon shell entangled with Co,N-co-doped carbon nanotubes. The as-prepared catalyst had a superior catalytic activity for oxygen evolution and oxygen reduction reactions, an ultralow potential gap of 0.74 V, and outstanding durability, surpassing most previous reports. Such superiority is ascribed, in part, to the unique three-dimensional electrode architecture of the composite, which is favourable for transporting oxygen species and electrons and creates a synergy between the components with different functionalities. Moreover, a flexible solid Zn-air battery assembled with such air electrode showed a steady discharge voltage plateau of 1.25 V and a round-trip efficiency of 70% at 1 mA cm^{-2}. This work presents a simple strategy to design highly efficient bifunctional oxygen electrocatalysts and may pave the way for the practical application of these materials in many energy conversion/storage devices.

1. Introduction

The rapid depletion of fossil fuels and severe environmental pollution from the use of these non-renewable energy resources have triggered intensive research activities on advanced energy conversion and storage systems. [1-3] Among these systems, rechargeable Zn-air batteries have a higher energy density and are more environmentally friendly compared to Li-ion batteries, and thus, rechargeable Zn-air batteries have been regarded as a more attractive alternative for use in next-generation energy storage systems. [4-8] However, in such electrochemical devices, the kinetics of the oxygen reduction reaction/oxygen evolution reaction (ORR/OER, corresponding to the discharge/charge processes) that occurs over the air electrode are slow, which greatly hinders the improvement of the overall energy-conversion efficiency and energy density of these devices. [9, 10] Currently, the noble metal Pt and metal oxides IrO_2 and RuO_2 have been widely used as the benchmark catalysts for ORRs and OERs, respectively. [11, 12] Although Pt, IrO_2, and RuO_2 have favourable activities, their scarcity, very expensive, and insufficient stability severely constrain the wide applications of these noble metal catalysts in Zn-air batteries. In addition, an individual noble metal catalyst is incapable of serving as a bifunctional electrocatalyst for both the ORR and OER. Thus, it is crucial to develop bifunctional oxygen catalysts that are inexpensive and highly durable and have high activities to realize their practical application in Zn-air batteries.

Until now, many researchers have focused on developing electrocatalysts with efficient dual active sites for both ORR and OER to integrate multiple active components. [13-17] For example, Liu *et al.* reported a bifunctional catalyst with a $NiCo_2S_4$ microsphere wrapped with a sulfur-doped graphene nanosheet. The catalyst had a favourable activity for both the ORR and OER because of the synergy between the sulfur-doped graphene nanosheets (which acted as ORR active sites) and $NiCo_2S_4$ microspheres (which acted as OER active sites). [13] Similarly, the use of a mesoporous Co_3O_4/ N-doped graphene oxide composite material as a bifunctional catalyst was also investigated, in which the synergistic effect of the N-doped graphene oxide towards the ORR and the Co_3O_4 nanosheets towards the OER was the critical factor for enhancing both the ORR and OER activities. [15] Although heteroatom-doped graphene was frequently utilized to improve the ORR activity, the high cost and poor dispersibility of graphene/graphene oxides limited their large-scale application.

Recently, metal-nitrogen-carbon (metal = Fe, Co, Ni, etc.) composites have been extensively reported as promising ORR electrocatalysts, owing to their cost competitiveness and high ORR catalytic activity. [18-22] According to Ma’s group, the designed N-doped carbon nanotubes with a FeCo nanoalloy delivered an extraordinarily high ORR activity, which was even superior to the state-of-the-art Pt/C benchmark. [21] Meanwhile, CoFe nanoparticles modified N-doped carbon nanotubes entangled with graphene oxide was also synthesized through chemical vapor deposition and possessed better ORR activities. [22] Particularly, the N-doped carbon nanotubes were also extensively researched and exhibited excellent ORR activities but inferior OER activities. [23-26] Based on these pioneering works, doping nitrogen into the carbon matrix structure is a method that can be used to regulate the distribution of electrons on the adjacent carbon atoms, which creates more effective active sites that improve the ORR activity. Compared to heteroatom-doped graphene and carbon nanotubes, the cost-effective N-doped carbon is a more promising ORR electrocatalyst for practical applications, because it is much less expensive and easier to mass produce.

In general, heteroatom-doped carbon materials possess superior ORR activities, while transition metal sulfides, oxides, and nitrides endow effective OER activities. [27-

29] Among the various OER catalysts, transition metal sulfides, particularly cobalt sulfides (CoS_x), have attracted much attention due to their favourable conductivities and superior OER activities compared to transition metal oxides and nitrides. [30-36] Therefore, creating catalysts by combining heteroatom-doped carbon and transition metal sulfides is an attractive technique for acquiring superior activity for both ORR and OER. For example, Dou *et al.* designed a two-step strategy to fabricate 2D bifunctional oxygen electrocatalysts, in which N-doped graphene was covered with Co_9S_8 nanoparticles. [33] Later, Han *et al*. prepared *in situ* 1D N-doped carbon nanotubes covered with $NiCo_2S_4$ nanocrystals by a two-step approach. [36] Disappointingly, covering the surface of N-doped carbon with metal sulfides diminished its ORR active sites, which mainly determine the power density and discharge energy density/capacity of a Zn-air battery. In addition, long direct exposures of metal sulfides in highly concentrated alkaline solution will passivate their OER activity and result in the poor cycle stability of the Zn-air battery. Furthermore, these low-dimensional (i.e., 1D and 2D) structure oxygen electrocatalysts are not favourable transporting O_2 species and electrons, due to the limited contact area between the solid electrocatalyst and the O_2-contained aqueous solution. In addition, the multi-step synthesis of the bifunctional catalysts was often time-consuming, costly, and difficult to scale-up for mass production. Therefore, developing high-performance bifunctional electrocatalysts by integrating transition metal sulfides and heteroatom-doped carbon with core-shell and 3D structures via a simple time- and cost-effective synthesis method is highly desirable.

Considering these points, we, for the first time, propose a scalable one-pot synthesis strategy based on self-catalysed chemical vapor deposition to fabricate a bifunctional electrocatalyst with a 3D sea urchin structure that consists of an ultrathin porous carbon nanosheet shell entangled with Co,N-co-doped carbon nanotube tails grown *in situ* on the surface of a CoS_x core (denoted as CoS_x/Co-NC). The optimal composite CoS_x/Co-NC-800 exhibited outstanding ORR and OER electrocatalytic activities in alkaline electrolytes (ΔE is only 0.74 V for CoS_x/Co-NC-800), as well as a superior cycling stability. Meanwhile, the synergistic improvement in the ORR/OER bifunctional activities resulting from the combination of CoS_x and Co-NC was also confirmed. Encouragingly, the CoS_x/Co-NC-800 bifunctional catalyst can be used in Zn-air batteries, as it demonstrated better rechargeability than the Pt/C and IrO_2 benchmarks. As a proof of concept, flexible rechargeable solid Zn-air batteries were assembled using CoS_x/Co-NC-800 as the air electrode, and these batteries had a steady discharge voltage platform of 1.25 V and a superior round-trip efficiency of 70% at 1 mA cm^{-2}. Moreover, the flexible Zn-air battery also exhibited a robust cycling stability with various degrees of bending.

2. Results and discussion

Figure 1 depicts the general procedure used for the preparation of the bifunctional CoSx/Co-NC catalyst, which was based on a facile one-pot carbonization process. Generally, $Co(NO_3)_2{\cdot}6H_2O$ was first mixed with thiourea, by hand grinding, to allow for sufficient coordination; during this process, the colour of the mixture turned from light red to dark blue. Then, melamine was added to the abovementioned ink-like product containing cobalt-thiourea complexes, ensuring that the complexes were uniformly embedded in the skeleton of melamine. After drying, the cobalt-thiourea complexes/melamine mixture was pyrolysed at 800 °C (or 700 °C or 900 °C) for 3 h under N_2 in a tube furnace. After heating the cobalt-thiourea complexes/melamine mixture to approximately 180 °C, the thiourea started to decompose and reacted with the cobalt salt to form CoS nucleuses (**Figure S1a**), and melamine remained in the composites. As the temperature reached 345-500 °C, melamine started to decompose and converted to graphitic carbon nitride (C_3N_4), and the encapsulated CoS nucleuses were converted to CoS_2 (**Figure S1b**). After the temperature finally reached 700-900 °C, the surface of CoS_2 was converted to Co via a reduction reaction with the carbon on C_3N_4, and then, C_3N_4 was further decomposed and catalysed by the Co nanoparticles to produce hybrids of N-doped carbon nanosheets and nanotubes on the CoS_x surface. Finally, acid leaching was performed to remove the undesired cobalt metal. The products obtained at the various temperatures were denoted as CoS_x/Co-NC-X (X= 700, 800 or 900 °C). For comparison, CoS_x and Co-NC were also prepared without adding melamine and thiourea, respectively, during the synthesis process.

Scanning electron microscopy (SEM) images show that the as-synthesized CoS_x-800 material has a smooth surface with particle sizes of approximately 3-10 μm **(Figures 2a and S2)**. In sharp contrast, the CoS_x/Co-NC-800 material has a rough surface consisted of sea urchin-like carbon nanotubes with diameters less than 100 nm (**Figures 2b, 2c and S3)**. X-ray diffraction (XRD) was used to probe the crystal structure of CoS_x/Co-NC-800 and CoS_x-800, respectively. Compared with pure CoS_x-800 (**Figure S4**), the as-prepared CoS_x/Co-NC-800 (**Figure 2d)** shows three well-defined peaks at 2-theta values of 29.8°, 47.6°, and 52.1°, which correspond to the (311), (511), and (440) facets of Co_8S_9. [35] Another diffraction peak located at a 2-theta of 44.2° corresponds to metallic Co, [37] which was embedded in the inner compartment of the carbon nanotubes. The transmission electron microscopy (TEM) images of CoS_x/Co-NC-800 further revealed that the carbon nanotubes with Co particles embedded in their inner compartments were *in situ* grown on the surface of the CoS_x nanoparticles (**Figures 2e and S5a)**, and these carbon nanotubes show characteristics of multi-walled structures with wall thickness of ~4 nm (**Figure 2f)**. **Figure S5b** shows that the CoS_x nanoparticles were partially wrapped with wrinkled graphene-like carbon nanosheets. According to the abovementioned SEM and TEM results, the as-prepared CoS_x/Co-NC-800 sample exhibited a unique 3D sea urchin structure, where carbon nanotubes and carbon nanosheets were *in situ* grown on the surface of CoS_x. Closer observation of the high-resolution transmission electron microscopy (HRTEM) images show that CoS_x/Co-NC-800 and CoS_x-800 have lattice spacings of 0.296 nm and 0.575 nm, which is consistent with the (311) and (111) plane of Co_8S_9, respectively (see **Figures 2g, 2h, S5c, S5d and S6**). More interestingly, a thin carbon layer with a lattice spacing of 0.35 nm (**Figures 2g and S5c**) was also observed on the surface of CoS_x/Co-NC-800, confirming that graphitization occurred; this agrees with the observation made based on **Figure S5b**.

The specific surface area and porous nature of CoS_x/Co-NC-800 was explored by obtaining a nitrogen adsorption-desorption isotherm, which was a type-IV isotherm with obvious hysteresis ($p/p_o > 0.45$), implying the presence of mesopores. The sharp nitrogen uptake in the high relative pressure region ($p/p_o \approx 0.99$) of the isotherm further confirms the co-existence of macropores. [38] The corresponding specific pore size distribution of CoS_x/Co-NC-800 (inset in **Figure 3a**) was analysed from the adsorption curve with the Barrett-Joyner-Halenda (BJH) equation, which showed that the average pore size was from 3.2 to 4.2 nm. The control samples pyrolysed at the other temperatures, 700 °C and 900 °C, also show similar structure parameters (**Figure S7**). Such an abundant porous structure enables the efficient transport of reaction species and easy contact with the electrolyte. Additionally, based on the isotherm, a high specific surface area of 95 $m^2\ g^{-1}$ was observed for the CoS_x/Co-NC-800 sample, which surpassed the specific surface areas of CoS_x/Co-NC-700 (27 $m^2\ g^{-1}$) and CoS_x/Co-NC-900 (69 $m^2\ g^{-1}$). For comparison, we also tested the specific surface area of the pure CoS_x-800 sample. As shown in **Figure 3a**, a negligible hysteresis was observed in the nitrogen adsorption-desorption isotherm, suggesting the lack of mesopores. CoS_x-800 had a much smaller specific surface area of 1.5 m^2 g^{-1}, which is only 1.59% of that of CoS_x/Co-NC-800 (95 m^2 g^{-1}). This suggests that the pores in CoS_x/Co-NC-800 mainly originated from the carbon phase. The phase composition of the samples was further analysed by Raman spectroscopy. As shown in **Figure 3b,** the peaks located at wavenumbers below 300 cm^{-1} are characteristic peaks of Co_9S_8, while the other peaks at 466, 507, and 673 cm^{-1} can be indexed to the E_g, F_{2g}, and A_{1g} modes of CoS, respectively. [39] Compared to CoS_x-800, two additional peaks characteristic of CoS_x/Co-NC appeared at 1335 cm^{-1} and 1590 cm^{-1}, which could be ascribed to defective carbon atoms (D band) and the sp^2-graphitic carbon (G band), respectively. The value of I_D/I_G (intensity ratio) is an important indicator of the graphitization degree of carbonaceous materials. [40, 41] The CoS_x/Co-NC sample has an I_D/I_G value of 1.029, indicating a high degree of carbon graphitization, which causes a high electrical conductivity; this is beneficial for applications of these materials as electrodes in energy storage and conversion systems. As the pyrolytic temperature increased, the I_D/I_G value of CoS_x/Co-NC decreased, implying that the graphitization degree was further enhanced (**Figure S8**); this conclusion agrees with previous reports. [41]

To obtain further insights into the surface chemical compositions and corresponding electronic structure of the CoS_x/Co-NC-800 and CoS_x-800 samples, X-ray photoelectron spectroscopy (XPS) measurements were conducted. The survey spectrum in **Figure S9** suggests the concomitance of cobalt, sulfur, carbon, oxygen, and nitrogen elements in CoS_x/Co-NC-800, whereas the CoS_x-800 sample was mainly composed of cobalt, sulfur, and oxygen elements. The corresponding specific atomic content of the CoS_x/Co-NC-800 and CoS_x-800 samples is listed in **Table S1**. The nitrogen content is approximately 8.8 *at.*% for CoS_x/Co-NC-800. The high-resolution

Co 2p spectrum of CoS_x/Co-NC-800 is presented in **Figure 3c** and could be deconvoluted into four doublets corresponding to metallic Co (778.2 and 793.0 eV), Co-S (778.5 and 793.8 eV), Co^{3+} (779.8 and 795.8 eV), and Co^{2+} (781.9 and 797.5 eV), and two satellite peaks corresponding to Co^{2+} were located at 785.1 and 802.6 eV. [27, 29, 41-43] The XPS Co 2p spectrum of CoS_x-800 shows similar peaks but without the metallic Co doublet. For the high-resolution S 2p spectrum of CoS_x-800 (**Figure 3d**), the peaks located at 161.4, 162.3, and 164.6 eV are ascribed to S^{2-} $2p_{3/2}$, S_2^{2-} $2p_{3/2}$, and S_n^{2-} $2p_{3/2}$, respectively, indicating the successful fabrication of the CoS_x phase. [27, 39, 44] The S 2p spectrum of CoS_x-800 is similar to that of CoS_x-800 but with different peak intensities (**Figure S10**). The appearance of oxygen in the CoS_x/Co-NC-800 and CoS_x-800 samples was attributed to the absorbed hydroxide species and partial oxidation of the material surface. The high-resolution C 1s spectra (**Figure 3e**) could be deconvoluted into five peaks located at 284.6, 285.7, 286.6, 288.9, and 291.4 eV, which can be assigned to bonded carbon atoms in -C-C-, C-N, C=N/C=O, O=C-O, and π-π*, respectively. The appearance of a peak attributed to C-N bonds demonstrated that the nitrogen atoms were successfully doped into the atomic skeleton of carbon. [45, 46] This was further confirmed by the high-resolution N 1s spectrum (**Figure 3f**), which could be deconvoluted into five peaks attributed to pyridinic-N (content: 36.76 *wt.*%, binding energy: 398.6 eV), Co-N_x (20.97 *wt.*%, 399.4 eV), pyrrolic-N (11.62 *wt.*%, 400.5 eV), graphitic-N (23.52 *wt.*%, 401.1 eV), and oxidized-N (7.13 *wt.*%, 402.6 eV). [17, 45] It is well known that electron-accepting pyridinic-N and graphitized-N with contents of approximately 61.12% can produce a positive charge on adjacent sp^2-hybridized carbon atoms, thus enhancing the reaction kinetics of the ORR. [12, 15, 37, 45] The doping of nitrogen into the carbon structure can regulate the surface properties and electronic structure of carbon materials to optimize the adsorption energy for various steps of electrochemical catalysis. [17, 37, 45] However, according to previous studies, the nitrogen content was decreased with increasing synthesis temperatures. [17, 37] Thus, the pyrolytic temperature should be optimized to balance the heteroatom doping and graphitization degree of carbon materials and achieve the optimal electrochemical performance.

Accordingly, we first evaluated the bifunctional oxygen electrocatalytic activity of the CoS_x/Co-NC samples pyrolysed at various temperatures. Linear sweep voltammetry (LSV) at rotating speeds of 1600 rpm was used to evaluate the activities of the ORR and OER for these samples in an O_2-saturated 0.1 M KOH electrolyte with a three-electrode system. As illustrated in **Figures S11** and **S12**, under nearly all conditions, CoS_x/Co-NC-800 has higher ORR and OER activities, including the half-wave, onset potential and limited current density, than CoS_x/Co-NC-700 and CoS_x/Co-NC-900. The CoS_x/Co-NC-700 sample had an inferior ORR performance with a half-wave potential at -3 mA cm^{-2} (defined as $E_{j=-3\ mA\ cm^{-2}}$) of 0.78 V, while CoS_x/Co-NC-800 and CoS_x/Co-NC-900 both had a half wave potential of 0.80 V at -3 mA cm^{-2}, possibly resulting from their slightly weak conductivities at a low pyrolytic temperature of 700 °C (**Figure S8**). The CoS_x/Co-NC-800 catalyst had the best OER performance with a low-operating potential at 10 mA cm^{-2} (defined as $E_{j=10\ mA\ cm^{-2}}$) of 1.54 V (vs RHE), and the catalyst with the next best OER performance was CoS_x/Co-NC-700 with a low-operating potential of 1.57 V (vs RHE) at 10 mA cm^{-2}. The CoS_x/Co-NC-900 sample had the worst performance with a low-operating potential of 1.62 V (vs RHE) at 10 mA cm^{-2}. The performance of these electrocatalysts at various pyrolytic temperatures was further assessed by the bifunctional parameter ΔE, which is defined as the difference between the potential of ORR at $E_{j=-3\ mA\ cm^{-2}}$ and the potential of OER at $E_{j=10\ mA\ cm^{-2}}$ (denoted as $\Delta E = E_{j=10\ mA\ cm^{-2}} - E_{j=-3\ mA\ cm^{-2}}$). A smaller ΔE means a better bifunctional catalytic activity. As shown in **Figure S13**, the optimal pyrolytic temperature was 800 °C. This trend in the activities of each of the catalysts may be due to CoS_x/Co-NC-800 having the largest specific surface area and a high conductivity, which could supply the catalyst with more active sites and improve the performance.

To demonstrate the superiority of CoS_x/Co-NC-800 as a bifunctional oxygen electrocatalyst, its catalytic activity was compared with the benchmark catalysts Pt/C (ORR) and IrO_2 (OER). CoS_x-800 and Co-NC-800 were also tested as other control samples. **Figure 4a** shows the representative ORR LSV curves for the CoS_x/Co-NC-800, CoS_x-800, Co-NC-800, Pt/C, and IrO_2 electrodes. As expected, because it is considered the OER benchmark, the IrO_2 electrode has a low OER activity, which agrees well with previous reports. [47, 48] The designed CoS_x/Co-NC-800 electrode, as expected, had superior ORR electrocatalytic activities; the onset potential (E_{onset}, 0.94 V) and half-wave potential ($E_{j=-3\ mA\ cm^{-2}}$, 0.80 V) of CoS_x/Co-NC-800 were much higher than those of CoS_x-800 (E_{onset} =0.77 V and $E_{j=-3\ mA\ cm^{-2}}$ = 0.60 V) and Co-NC-800 (E_{onset} =0.88 V and $E_{j=-3\ mA\ cm^{-2}}$ = 0.78 V) and even approached the E_{onset} and $E_{j=-3\ mA\ cm^{-2}}$ of commercial Pt/C catalysts (0.98 V and 0.82 V, respectively). In addition, the limiting current density at 0.4 V (vs RHE) of the CoS_x/Co-NC-800 (5.23 mA cm^{-2}), commercial Pt/C (5.14 mA cm^{-2}), CoS_x-800 (4.40 mA cm^{-2}), and Co-NC-800 (5.11 mA cm^{-2}) electrodes also followed the same trend. This implies that the ORR activity of CoS_x/Co-NC-800 primarily originated from Co-NC, which agrees with the previous study. Next, the ORR mechanism of the as-prepared CoS_x/Co-NC-800 catalysts was further investigated. As shown by the LSV curves in **Figure S14a, c**, the limited current densities of the Pt/C and CoS_x/Co-NC-800 catalysts were improved by increasing the rotating speed, demonstrating that the ORR was diffusion-limited. The good linearity of the Koutecky-Levich (K-L) plots for a potential range from 0.5 to 0.7 V (**Figures S14b, d**) indicates that oxygen reacts in the alkali electrolyte by first-order reaction kinetics. In addition, the calculated electron transfer number (n) for the CoS_x/Co-NC-800 catalyst is 3.96, which is approaching that of Pt/C (4.0); this demonstrates the existence of an efficient $4e^-$ reduction pathway. Similarly, the LSV curves and K-L plots for other control samples were also exhibited in **Figure S15 and S16**. As shown in **Figure 4b**, the Tafel plots were converted from the LSV curves of the ORR near the onset potential. A Tafel slope of 67 mV dec^{-1} was observed for the commercial Pt/C catalyst, which agrees well with the previous reports. [34, 35] Interestingly, the CoS_x/Co-NC-800 catalyst had a Tafel slope of 62 mV dec^{-1}, which was lower than the Tafel slope of CoS_x-800 (115 mV dec^{-1}) and Co-NC-800 (73 mV dec^{-1}). All the aforementioned superior characteristics of CoS_x/Co-NC-800, relative to CoS_x-800 and Co-NC-800, were likely due to its unique 3D structure, which facilitated the diffusion of oxygen on the catalyst surface and enhanced the ORR performance of this composite, as well as the synergy between the two phases. [22]

The long-term durability of the catalysts was another critical factor for practical applications, such as in metal–air batteries. The ORR stability of the optimal CoS_x/Co-NC-800 and commercial Pt/C catalysts were then compared by performing current–time (i–t) chronoamperometry measurements at a constant potential of 0.3 V (vs RHE) for 12 h. (**Figure 4c**). The CoS_x/Co-NC-800 catalyst shows only a minor loss of its original current (8.5%) after operating for 12 h, which is much better than the 35.9% loss incurred by the commercial Pt/C catalyst; this suggests that the stability of CoS_x/Co-NC-800 is superior to that of the commercial Pt/C catalyst.

To evaluate the bifunctionality, the OER electrocatalytic performance of these catalysts was further investigated by performing LSV in an O_2-saturated 0.1 M KOH electrolyte at 1600 rpm. **Figure 4d** displays the LSV curves for the OER on CoS_x/Co-NC-800, Pt/C, IrO_2, CoS_x-800, and Co-NC-800. Similar to the behaviour observed for

IrO_2 when used as an ORR catalyst, Pt/C, when used as an OER catalyst, had a poor catalytic activity, which agrees with the previous reports. [22, 36] Pure CoS_x had an outstanding OER catalytic activity; its onset potential (E_{onset}) and operating potential at a current density of 10 mA cm^{-2} (defined as $E_{j=10\ mA\ cm^{-2}}$) were 1.47 and 1.55 V (vs RHE), respectively, which are approaching the E_{onset} and $E_{j=10\ mA\ cm^{-2}}$ of the CoS_x/Co-NC-800 composites ($E_{j=onset}$, $E_{j=10\ mA\ cm^{-2}}$). Co-NC-800 had a much inferior OER activity relative to CoS_x. This observation confirmed that CoS_x acted as the main OER active site. More significantly, compared to all the control samples, the CoS_x/Co-NC-800 composites demonstrated the highest current density for a range of potentials, the lowest E_{onset} of 1.46 V, and the lowest potential at $E_{j=10\ mA\ cm^{-2}}$ of 1.54 V (vs RHE), and these values were even much lower than those of the noble metal IrO_2 (E_{onset} = 1.47 V, $E_{j=10\ mA\ cm^{-2}}$ = 1.69 V), suggesting that the CoS_x/Co-NC-800 composite had an unprecedented OER catalytic activity. The OER kinetics were studied by preparing Tafel plots. The CoS_x/Co-NC-800 catalyst had a Tafel slope of 96 mV dec^{-1}, which was lower than that of CoS_x-800 (100 mV dec^{-1}) and Co-NC-800 (108 mV dec^{-1}) (**Figure 4e**); this result further proved the superior OER activities of CoS_x/Co-NC-800. [42] The EIS Nyquist plots in **Figure S17** show that the CoS_x/Co-NC-800 catalyst has the lowest charge transfer impedance. **Figure S17** further confirmed that the unique 3D structure favoured electron transport, which accelerated the OER. Last, the long-term durability of OER was also tested at a constant current density of 10 mA cm^{-2} for 20000 s (**Figure 4f**). The CoS_x/Co-NC-800 catalyst maintained its initial potential after 20000 s of continuous testing; the performance of the CoS_x/Co-NC-800 catalyst surpassed that of the noble metal IrO_2 catalyst, which was only stable for 2500 s.

The outstanding bifunctionality of the CoS_x/Co-NC-800 oxygen electrocatalyst was further confirmed by evaluating ΔE. As exhibited in **Figure 5a**, the CoS_x/Co-NC-800 catalyst had the lowest ΔE (ΔE = 0.74 V) among the noble metal catalysts and the comparative catalysts, implying the presence of a synergistic effect between CoS_x (with its excellent OER performance) and Co-NC (with its excellent ORR performance) in the composite. More importantly, we also compared the ΔE of the noble metal catalysts (IrO_2 and Pt/C) with previous research to ensure the validity of our work (**Table S2**). The bifunctional catalytic activity of our work was compared with that of recently reported catalysts based on the composites of transition metals and heteroatom-doped carbon, and **Figure 5b** shows the excellent performance of CoS_x/Co-NC-800 (detail information shown in **Table S3**).

Based on the abovementioned analysis combined with the previous reports, the extraordinary ORR/OER activities of CoS_x/Co-NC-800 are attributed to its unique 3D sea urchin structure, which is advantageous for transferring O_2*/OH* species and electrons. [22] As shown in **Figure 5c**, the current in the electrode was diffusion-limited during the ORR and mainly depended on the existence of an oxygen concentration gradient near the catalyst surface, causing the heterogeneous catalysis. Namely, the key factor driving the ORR process is the dissolved oxygen in the electrolyte, which penetrates the depletion layer to reach the solid catalyst surface. [49] In the case of a 3D sea urchin structure such as CoS_x/Co-NC, the N-doped carbon nanotubes could act as tentacles to capture oxygen in the oxygen-saturated electrolyte, thus facilitating the transport of oxygen species across the depletion layer and the absorption of these species on the surface of the catalyst. During the OER process, as described in **Figure 5d**, the oxygen evolution reaction mainly occurred on the surface of the CoS_x core, and the abundant nanopores on the surface of the encapsulated ultrathin carbon shell allowed the rapid OER process to occur, causing the oxidization of OH^- to O_2. Typically, the OER performance in alkaline solution was also affected by O_2 desorption.

Fortunately, the tentacle-liked N-doped carbon nanotubes that were *in situ* grown on CoS_x/Co-NC are beneficial to rapidly transporting the produced O_2 species into the electrolyte. [22, 49] In addition, the 3D carbon structure could serve as a conductive network to reduce the charge transfer impedance during the OER process (**Figure S17**), thus improving the oxygen evolution reaction kinetics.

Zn-air batteries are prospective energy storage devices due to their high theoretical specific capacities and intrinsic safety. The performance of the designed bifunctional catalysts in real Zn-air battery was investigated. A Zn-air battery was fabricated using carbon sheets coated with a CoS_x/Co-NC-800 catalyst (1 mg cm^{-2}) as the air electrode, Zn foil as the anode, and a 6 M KOH and 0.2 M $ZnCl_2$ aqueous solution as the electrolyte (**Figure 6a, S18**). For comparison, a primary Zn-air battery composed of a noble metal Pt/C catalyst (1 mg cm^{-2}) and a rechargeable Zn-air battery composed of a mixture of Pt/C and IrO_2 (with a 1:1 weight ratio, where the total amount of the active materials was 1 mg cm^{-2}), used as the air electrode, were also fabricated and investigated.

A digital photograph of the three homemade Zn-Air batteries is shown in **Figure 6b** and was used to determine the open circuit voltage of 4.19 V (~1.40 V for each single cell). The polarization curves of CoS_x/Co-NC-800 and Pt/C are shown in **Figure 6c**. These polarization curves show that the discharge voltages obtained using CoS_x/Co-NC-800 as the air cathode were 1.25, 1.07 and 0.87 V at 10, 50 and 100 mA cm^{-2}, respectively, while the discharge voltages obtained using Pt/C as the air cathode were 1.25, 1.03 and 0.79 V at 10, 50 and 100 mA cm^{-2}, which shows that using CoS_x/Co-NC-800 as the air cathode results in discharge voltages comparable to Pt/C. Moreover, the maximum power densities of the battery with CoS_x/Co-NC-800 and the battery with the noble metal Pt/C catalyst were 103 mW cm^{-2} at 165 mA cm^{-2} and 87 mW cm^{-2} at

147 mA cm^{-2}, respectively, and thus, the battery with CoS_x/Co-NC-800 outperformed the battery with the noble metal Pt/C catalyst. At a discharge current density of 10 mA cm^{-2}, the battery with the CoS_x/Co-NC-800 cathode exhibited a high specific capacity (per g of Zn) of 770.4 mAh g_{Zn}^{-1} (retaining 94.0% of the theoretical capacity, 820 mAh g_{Zn}^{-1}) (**Figure 6d**) and a high energy density (per kg of Zn) of 923.5 Wh kg_{Zn}^{-1} (**Figure S19**), which surpasses the specific capacity and energy density of Pt/C (744.7 mAh g_{Zn}^{-1} and 860.0 Wh kg_{Zn}^{-1}). In addition, the discharge capacity at high current densities was also obtained for the CoS_x/Co-NC-800 catalyst. As shown in **Figures 6d and S19**, the batteries had specific capacities of 752.7 and 734.2 mAh g_{Zn}^{-1} at 20 and 40 mA cm^{-2}, respectively, corresponding to energy densities of 858.1 and 735.4 Wh kg_{Zn}^{-1}, respectively. These values are also comparable or even superior to those of the previously reported catalysts (**Table S4**). The excellent specific capacity of the CoS_x/Co-NC-800 catalyst at a high current density was derived from the excellent conductivity of the carbon sheets and carbon nanotubes on the surface, which effectively improved the electron transport between the catalyst particles. Then, the primary Zn-air battery with the CoS_x/Co-NC-800 air electrode could be mechanically recharged by replacing the spent anode with a fresh Zn anode. As shown in **Figure S20**, the specific capacity did not decline after the battery was mechanically recharged five times with a total period of operation at 10 mA cm^{-2} of approximately 183 h. More importantly, after the battery was mechanically recharged five times, 97.1% of the initial capacity was still retained (**Figure 6e**), demonstrating the remarkable long-term durability of the CoS_x/Co-NC-800 catalyst for the ORR in a practical cell/battery. All the capacities were normalized to the mass of consumed zinc. Interestingly, the three Zn-air batteries with the CoS_x/Co-NC-800 air electrode connected in series could power

an LED viewing screen for 12 h without any change in the brightness of the LED screen (**Figure 6f**), demonstrating that the batteries could be applied in practical power devices.

Then, the rechargeable Zn-air battery was further evaluated by a galvanostatic charge/discharge test. When cycled at 2 mA cm^{-2}, as shown in **Figure S21a**, the first charge and discharge voltages of the battery with the CoS_x/Co-NC-800 air electrode were 1.24 and 1.97 V, respectively; the battery with the CoS_x/Co-NC-800 air electrode had a low discharge/charge polarization of only 0.73 V and an excellent round-trip efficiency of 62.9%, which were better than the discharge/charge polarization and round-trip efficiency of the battery with the noble metal Pt/C + IrO_2 air electrode, 0.79 V and 61.2%, respectively (the first charge and discharge voltages were 1.25 V and 2.04 V, respectively). After the battery was operated for 100 h, the charge/discharge polarization of the CoS_x/Co-NC-800 air electrode only increased by approximately 60 mV, and the round-trip efficiency slightly decreased to 61.1%, making the CoS_x/Co-NC-800 air electrode obviously superior to the Pt/C + IrO_2 air electrode; after the battery was operated for 70 h, the discharge/charge polarization and round-trip efficiency of the Pt/C + IrO_2 air electrode were 1.26 V and 48.5%, respectively. The cycling performances at 2 mA cm^{-2} for both the Pt/C + IrO_2 mixture and CoS_x/Co-NC-800 air electrodes are presented in **Figure 6g**, which shows that the battery with the CoS_x/Co-NC-800 air electrode could continuously operate for 200 h without any obvious decay in the performance. In addition, the cycling performance of the battery with the CoS_x/Co-NC-800 air electrode was also performed at 5 mA cm^{-2}. The battery with the CoS_x/Co-NC-800 air electrode was stable after 450 cycles (*ca.* 90 h, 12 min for one cycle), and the corresponding discharge/charge curve is shown in **Figure 6h**. The performance of CoS_x/Co-NC-800 and Pt/C + IrO_2 at 5 mA cm^{-2} were also compared, as shown in **Figure S21b**. After testing, the voltage polarization only increased by approximately 44 mV, which is substantially lower than the voltage polarization of 566 mV obtained for the Pt/C + IrO_2 mixture (**Figure S21c**); this confirms the outstanding ORR/OER activities and excellent structural stability of the CoS_x/Co-NC-800 air electrode under practical operating conditions.

Based on the excellent performance of the aqueous Zn-air battery, a flexible rechargeable solid Zn-air battery was assembled comprising a carbon sheet loaded with CoS_x/Co-NC-800 (~2 mg cm^{-2}) (acting as the air electrode), nickel foam (acting as the current collector), an alkaline gel polymer electrolyte (acting as the separator), and a zinc foil (acting as the anode) (**Figure 7a**). A digital photograph of the flexible battery is shown in **Figure 7b**, and the open circuit voltage of the flexible battery is 1.34 V. In addition, three flexible batteries were used to power an LED viewing screen (**Figure 7c**), demonstrating the significant potential of the reported catalyst. **Figure S22** shows the discharging-charging curve of the flexible solid battery at 1 mA cm^{-2} for 100 cycles (where each cycle was 10 min). The flexibility was further evaluated, as shown in **Figure 7d**. The discharge/charge voltage plateaued at 1 mA cm^{-2}, even when the battery was bent at various angles (including 90° and 180°). At an initial condition of 0°, an ultralow voltage polarization of 0.54 V and a high round-trip efficiency of 70% were obtained for the flexible solid battery (the charge and discharge voltages were 1.79 V and 1.25 V, respectively). A low voltage polarization and high round-trip efficiency were achieved at 90° (0.54 V, 70%) and 180° (0.58 V, 68%); a voltage polarization of 0.63 V and round-trip efficiency of 65.8% were achieved after the battery was restored to its initial condition, showing the excellent flexibility of the prepared solid battery. Hence, these results, including those of the Zn-air battery and the flexible rechargeable solid battery, effectively demonstrated that the CoS_x/Co-NC-800 catalyst could be a new high-performance ORR and OER catalyst for actual applications in Zn-air batteries.

The desirable performance of the Zn-air battery based on the CoS_x/Co-NC-800 catalyst is ascribed to its unique 3D structure. The self-catalysed chemical vapor deposition renders a composite of CoS_x and N-doped porous carbon with a core-shell structure. The interaction between CoS_x and the N-doped porous carbon was observed in the unique structure of the prepared catalyst. Moreover, covering the surface of CoS_x with multi-layer porous carbon nanosheets and carbon nanotubes could accelerate the transfer of oxygen species and electrons, causing the desirable activities necessary for the excellent performance of the Zn-air battery. Further study is required to design a catalyst with a macroporous structure, which can act as transport channels for oxygen bubbles. The as-prepared catalyst is also important for many potential energy applications, such as water splitting, [50] Li-O_2 batteries, [51] Li/Na-ion batteries, [39] etc.

3. Conclusions

In summary, composites of a CoS_x particle core embedded in a porous graphene-like carbon shell covered with Co, N-doped carbon nanotubes was successfully prepared by a scalable one-pot method based on self-catalysed chemical vapor deposition. The material showed excellent ORR/OER activities ($\Delta E = 0.74$ V) and an improved durability compared to the individual components, CoS_x and Co,N-co-doped carbon nanotubes, due to a synergistic effect, making this composite useful for application as an oxygen electrocatalyst. The primary Zn-air battery has a high specific capacity and a high energy density and exhibited excellent stability after mechanically recharging five times and operating for approximately 183 h at 10 mA cm^{-2}. In addition, the rechargeable battery also exhibited better cycle performance than the benchmark materials, the Pt/C mixture and IrO_2. Therefore, this work reports a rational and low-cost strategy to design efficient bifunctional catalysts for energy storage and conversion devices. As a proof of concept, a flexible rechargeable solid battery was assembled with

CoS_x/Co-NC-800 and exhibited an excellent cycling performance and a good round-trip efficiency, even under bending conditions.

Supporting Information

Supporting Information is available from the Wiley Online Library or from the author.

Acknowledgements

Z. Shao and K. Liao thank the funding support provide by the National Key R&D Program of China (No. 2018YFB0905400); K. Liao thanks the funding support provided by the National Natural Science Foundation of China (No. 51802152) and the Natural Science Foundation of Jiangsu Province of China (No. BK20170974).

Received: ((will be filled in by the editorial staff))
Revised: ((will be filled in by the editorial staff))
Published online: ((will be filled in by the editorial staff))

Figures and captions

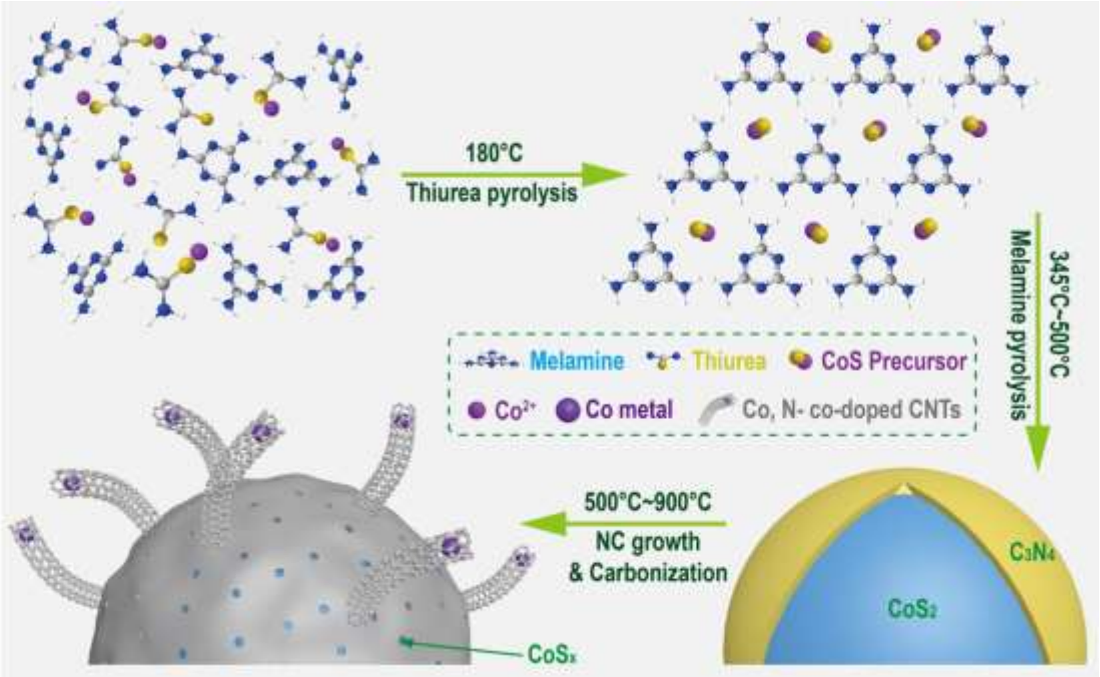

Figure 1. Illustrated formation procedures of the CoS_x/Co-NC.

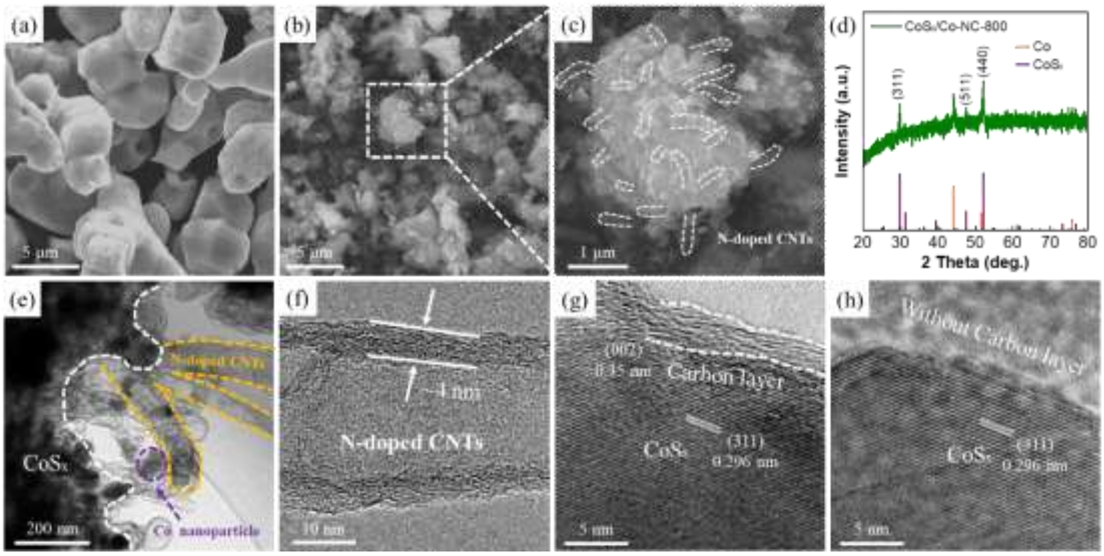

Figure 2. SEM images of (a) CoS_x-800; (b, c) CoS_x/Co-NC-800; (d) X-ray diffraction pattern of the CoS_x/Co-NC-800; (e, f) TEM images of CoS_x/Co-NC-800; HRTEM images of (g) CoS_x/Co-NC-800; (h) CoS_x-800.

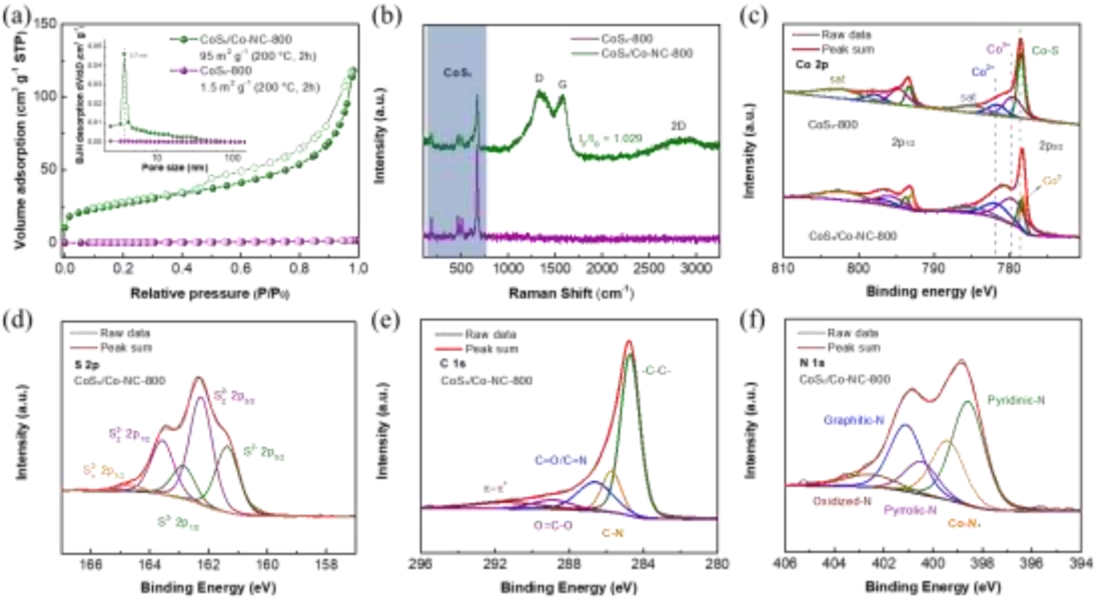

Figure 3. (a) Nitrogen adsorption-desorption isotherm of CoS_x-800 and CoS_x/Co-NC-800 (pore size distribution exhibited in inset); (b) raman scattering spectra of CoS_x-800 and CoS_x/Co-NC-800; (c) the comparison of Co 2p XPS spectra of CoS_x-800 (upper) and CoS_x/Co-NC-800 (bottom); elemental XPS spectra of CoS_x/Co-NC-800: (d) high-resolution S 2p; (e) high-resolution C 1s; and (f) high-resolution N 1s.

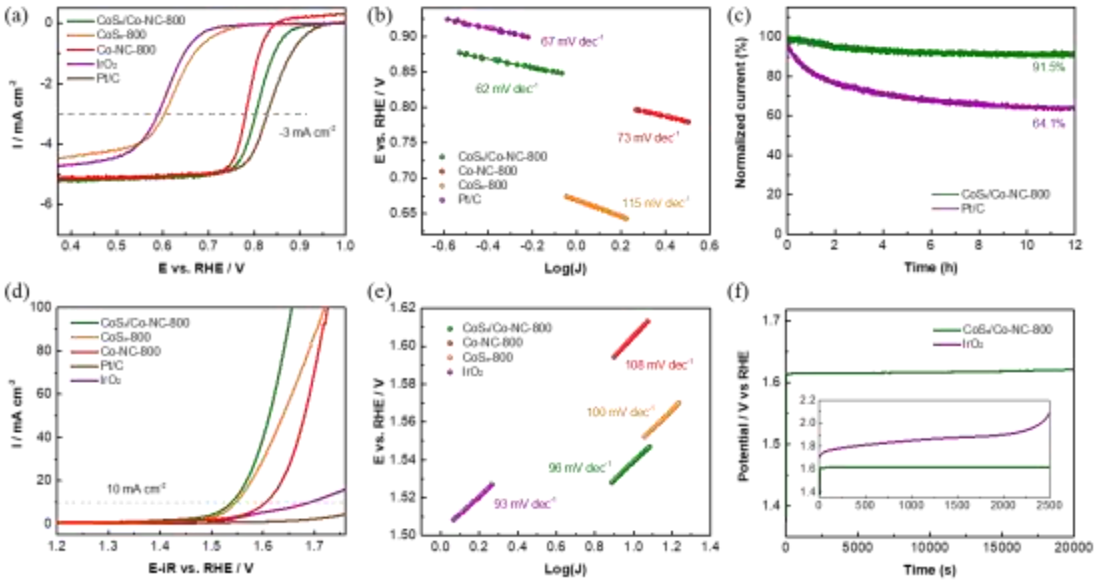

Figure 4. (a) LSV curves of ORR; (b) Tafel plots for ORR; (c) chronoamperometric response of ORR at 0.30 V; (d) LSV curves of OER; (e) Tafel plots for OER; (f) OER durability at 10 mA cm^{-2}. Above data were collected in the O_2-saturated 0.1 M KOH at 1600 rpm with 5 mV s^{-1}.

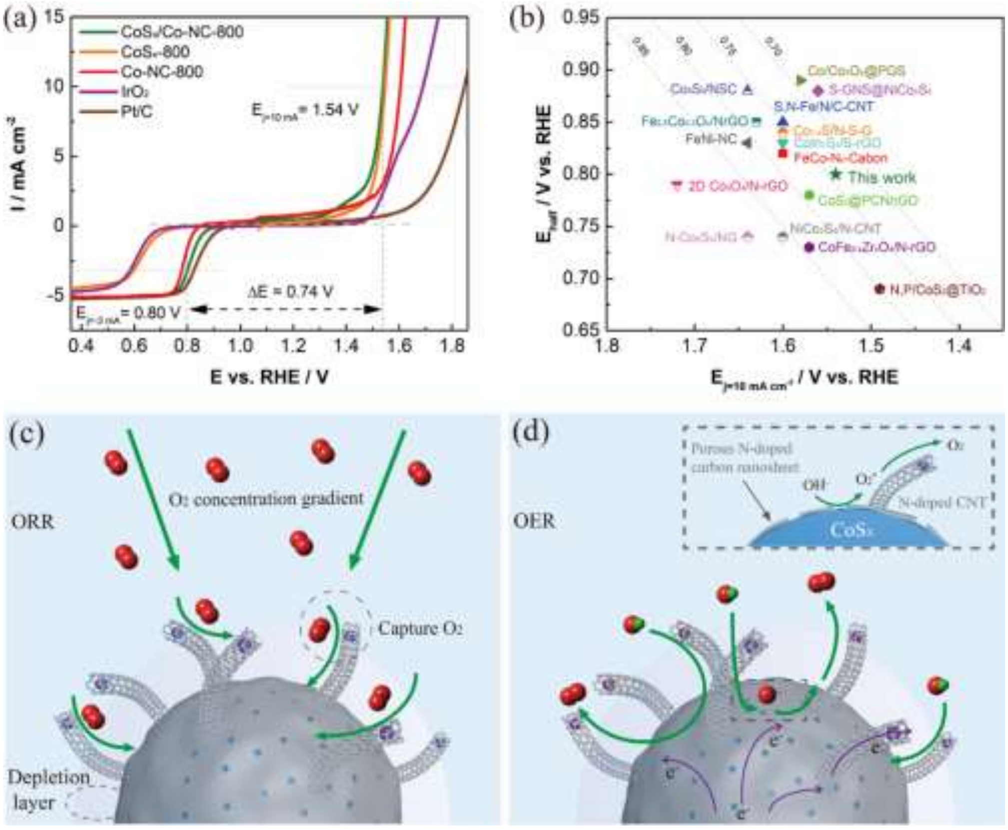

Figure 5. (a) The overall LSV curves of different catalysts; (b) the comparison of ORR and OER overpotentials for reported catalysts with this work ($\Delta E = E_{j=10mA\ cm^{-2}} - E_{j=-3mA\ cm^{-2}}$); (c, d) mechanism of ORR and OER for synergistic effect in the CoS_x/Co-NC-800 composites.

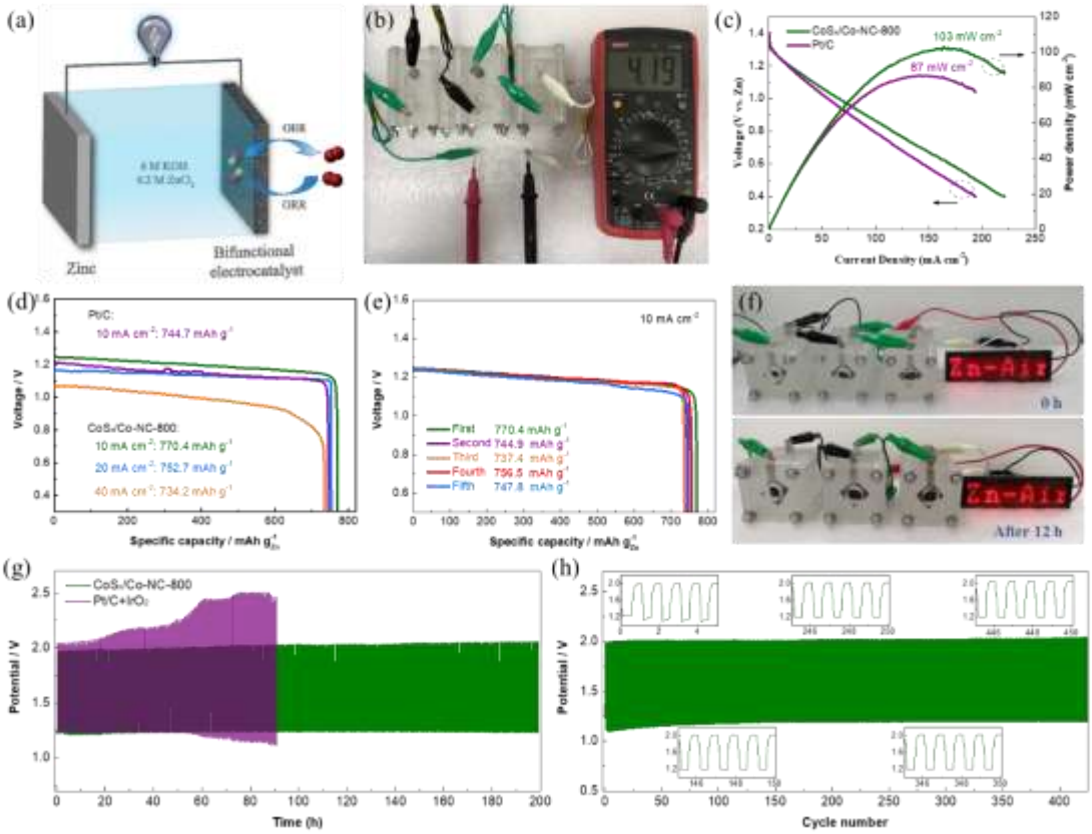

Figure 6. (a) Diagram of zinc-air battery; (b) photograph of three tandem home-made Zn-Air batteries; (c) polarization (V-j) curves and power density (P-j) curves based on the Pt/C catalyst and CoS_x/Co-NC-800 catalyst, respectively; galvanostatic discharge voltage-capacity curves for (d) different current densities, and (e) permanent current densities; (f) three home-made rechargeable Zn-Air battery connected in series used to power a LED screen; galvanostatic charge/discharge test: (g) built with Pt/C + IrO_2 catalyst and CoS_x/Co-NC-800 catalyst, and (f) built with CoS_x/Co-NC-800 catalyst and corresponding charge-discharge curves.

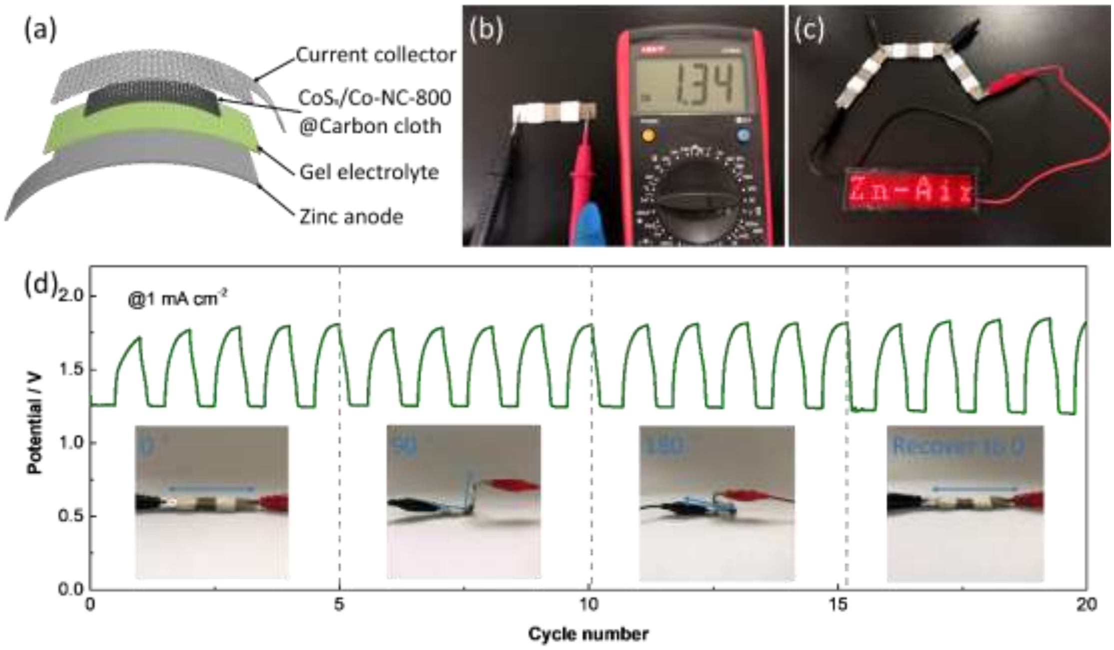

Figure 7. (a) Diagram of the flexible solid zinc-air battery; (b) photograph of the flexible battery with an OCV of 1.34 V; (c) three flexible solid batteries connected in series used to lighten a LED screen; (d) discharging-charging curve of flexible battery under different bending conditions at 1 mA cm^{-2} (6 min for each cycle).

References

[1] Y. Li, H. Dai, *Chem. Soc. Rev.* **2014**, *43*, 5257.

[2] S. Chu, Y. Cui, N. Liu, *Nat. Mater.* **2016**, *16*, 16.

[3] K. Liao, S. Wu, X. Mu, Q. Lu, M. Han, P. He, Z. Shao, H. Zhou, *Adv. Mater.* **2018**, *30*, 1705711.

[4] J. Yi, P. Liang, X. Liu, K. Wu, Y. Liu, Y. Xia, J. Zhang, *Energy Environ. Sci.* **2018**, *11*, 3075.

[5] J. Fu, Z. P. Cano, M. G. Park, A. Yu, M. Fowler, Z. Chen, *Adv. Mater.* **2017**, *29*, 1604685.

[6] Y. Zhong, X. Xu, W. Wang, Z. Shao, *Batteries & Supercaps* **2019**, *2*, 272.

[7] X. Zou, Q. Lu, Y. Zhong, K. Liao, W. Zhou, Z. Shao, *Small* **2018**, *14*, 1801798.

[8] P. Tan, B. Chen, H. Xu, W. Cai, W. He, M. Ni, *Appl. Catal. B: Environ.* **2019**, *241*, 104.

[9] D. Zhou, Y. Jia, H. Yang, W. Xu, K. Sun, J. Zhang, S. Wang, Y. Kuang, B. Liu, X. Sun, *J. Mater. Chem. A* **2018**, *6*, 21162.

[10] Y. Zhao, J. Zhang, W. Wu, X. Guo, P. Xiong, H. Liu, G. Wang, *Nano Energy* **2018**, *54*, 129.

[11] G. Fu, J. Wang, Y. Chen, Y. Liu, Y. Tang, J. B. Goodenough, J.-M. Lee, *Adv. Energy Mater.* **2018**, *8*, 1802263.

[12] Z. Pei, Z. Tang, Z. Liu, Y. Huang, Y. Wang, H. Li, Q. Xue, M. Zhu, D. Tang, C. Zhi, *J. Mater. Chem. A* **2018**, *6*, 489.

[13] W. Liu, J. Zhang, Z. Bai, G. Jiang, M. Li, K. Feng, L. Yang, Y. Ding, T. Yu, Z. Chen, A. Yu, *Adv. Funct. Mater.* **2018**, *28*, 1706675.

[14] L. Wei, H. E. Karahan, S. Zhai, H. Liu, X. Chen, Z. Zhou, Y. Lei, Z. Liu, Y. Chen, *Adv. Mater.* **2017**, *29*, 1701410.

[15] Y. Li, C. Zhong, J. Liu, X. Zeng, S. Qu, X. Han, Y. Deng, W. Hu, J. Lu, *Adv. Mater.* **2018**, *30*, 1703657.

[16] Y. Bu, G. Nam, S. Kim, K. Choi, Q. Zhong, J. Lee, Y. Qin, J. Cho, G. Kim, *Small* **2018**, *14*, 1802767.

[17] W. Zhang, X. Yao, S. Zhou, X. Li, L. Li, Z. Yu, L. Gu, *Small* **2018**, *14*, 1800423.

[18] Y. Zhang, L. Lu, S. Zhang, Z. Lv, D. Yang, J. Liu, Y. Chen, X. Tian, H. Jin, W. Song, *J. Mater. Chem. A* **2018**, *6*, 5740.

[19] L. T. Song, Z. Y. Wu, F. Zhou, H. W. Liang, Z. Y. Yu, S. H. Yu, *Small* **2016**, *12*, 6398.

[20] Z. Hu, Z. Guo, Z. Zhang, M. Dou, F. Wang, *ACS Appl. Mater. Interfaces* **2018**, *10*, 12651.

[21] C.-Y. Su, H. Cheng, W. Li, Z.-Q. Liu, N. Li, Z. Hou, F.-Q. Bai, H.-X. Zhang, T.-Y. Ma, *Adv. Energy Mater.* **2017**, *7*, 1602420.

[22] X. Liu, L. Wang, P. Yu, C. Tian, F. Sun, J. Ma, W. Li, H. Fu, *Angew. Chem. Int. Ed.* **2018**, *57*, 16166.

[23] X. Wan, R. Wu, J. Deng, Y. Nie, S. Chen, W. Ding, X. Huang, Z. Wei, *J. Mater. Chem. A* **2018**, *6*, 3386.

[24] S. Liu, I. S. Amiinu, X. Liu, J. Zhang, M. Bao, T. Meng, S. Mu, *Chem. Eng. J.* **2018**, *342*, 163.

[25] L. Ma, R. Wang, Y.-H. Li, X.-F. Liu, Q.-Q. Zhang, X.-Y. Dong, S.-Q. Zang, *J. Mater. Chem. A* **2018**, *6*, 24071.

[26] T. Li, H. Deng, J. Liu, C. Jin, Y. Song, F. Wang, *Carbon* **2019**, *143*, 859.

[27] W. Niu, Z. Li, K. Marcus, L. Zhou, Y. Li, R. Ye, K. Liang, Y. Yang, *Adv. Energy Mater.* **2018**, *8*, 1701642.

[28] P. Tan, B. Chen, H. Xu, W. Cai, W. He, M. Liu, Z. Shao, M. Ni, *Small* **2018**, *14*, 1800225.

[29] C. Guan, A. Sumboja, W. Zang, Y. Qian, H. Zhang, X. Liu, Z. Liu, D. Zhao, S. J. Pennycook, J. Wang, *Energy Storage Mater.* **2019**, *16*, 243.

[30] P. Cai, J. Huang, J. Chen, Z. Wen, *Angew. Chem. Int. Ed.* **2017**, *56*, 4858.

[31] X. Zhao, J. Jiang, Z. Xue, C. Yan, T. Mu, *Chem. Commun.* **2017**, *53*, 9418.

[32] B. Liu, S. Qu, Y. Kou, Z. Liu, X. Chen, Y. Wu, X. Han, Y. Deng, W. Hu, C. Zhong, *ACS Appl. Mater. Interfaces* **2018**, *10*, 30433.

[33] S. Dou, L. Tao, J. Huo, S. Wang, L. Dai, *Energy Environ. Sci.* **2016**, *9*, 1320.

[34] X. Qiao, J. Jin, H. Fan, Y. Li, S. Liao, *J. Mater. Chem. A* **2017**, *5*, 12354.

[35] Z.Q. Cao, M.Z. Wu, H.B. Hu, G.J. Liang, C.Z. Zhi, *NPG Asia Mater.* **2018**, *10*, 670.

[36] X. Han, X. Wu, C. Zhong, Y. Deng, N. Zhao, W. Hu, *Nano Energy* **2017**, *31*, 541.

[37] H. Jiang, Y. Liu, W. Li, J. Li, *Small* **2018**, *14*, 1703739.

[38] Y. Zhong, Q. Lu, Y. Zhu, Y. Zhu, W. Zhou, S. Wang, Z. Shao, *Adv. Sustainable Syst.* **2017**, *1*, 1700081.

[39] B. Yin, X. Cao, A. Pan, Z. Luo, S. Dinesh, J. Lin, Y. Tang, S. Liang, G. Cao, *Adv. Sci.* **2018**, *5*, 1800829.

[40] S. Wei, S. Chu, Q. Lu, W. Zhou, R. Cai, Z. Shao, *ChemistrySelect* **2018**, *3*, 4015.

[41] Z. Guo, F. Wang, Y. Xia, J. Li, A. G. Tamirat, Y. Liu, L. Wang, Y. Wang, Y. Xia, *J. Mater. Chem. A* **2018**, *6*, 1443.

[42] H. Yang, B. Wang, H. Li, B. Ni, K. Wang, Q. Zhang, X. Wang, *Adv. Energy Mater.* **2018**, *8*, 1801839.

[43] H. F. Wang, C. Tang, B. Wang, B. Q. Li, Q. Zhang, *Adv. Mater.* **2017**, *29*, 1702327.

[44] Q. Lu, Y. Sun, K. Liao, X. Zou, I. Hamada, W. Zhou, M. Ni, Z. Shao, *Electrochim. Acta* **2019**, *298*, 421.

[45] C. Tang, B. Wang, H. F. Wang, Q. Zhang, *Adv. Mater.* **2017**, *29*, 1703185.

[46] Q. Lu, Y. Zhong, W. Zhou, K. Liao, Z. Shao, *Adv. Mater. Interfaces* **2018**, *5*, 1701659.

[47] Y. Li, J. Yin, L. An, M. Lu, K. Sun, Y. Q. Zhao, F. Cheng, P. Xi, *Nanoscale* **2018**, *10*, 6581.

[48] A. Aijaz, J. Masa, C. Rosler, W. Xia, P. Weide, A. J. Botz, R. A. Fischer, W. Schuhmann, M. Muhler, *Angew. Chem. Int. Ed.* **2016**, *55*, 4087.

[49] P. Chen, T. Zhou, L. Xing, K. Xu, Y. Tong, H. Xie, L. Zhang, W. Yan, W. Chu, C. Wu, Y. Xie, *Angew. Chem. Int. Ed.* **2017**, *56*, 610.

[50] Y. Liu, Q. Li, R. Si, G. D. Li, W. Li, D. P. Liu, D. Wang, L. Sun, Y. Zhang, X. Zou, *Adv. Mater.* **2017**, *29*, 1606200.

[51] P. Sennu, M. Christy, V. Aravindan, Y. G. Lee, K. S. Nahm, Y. S. Lee, *Chem. Mater.* **2015**, *27*, 5726.

TOC figure:

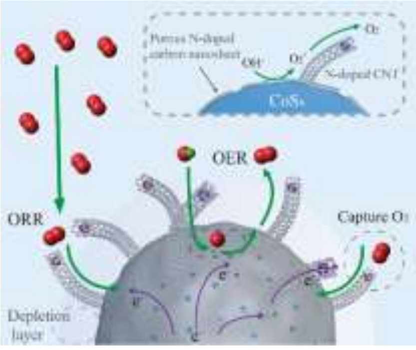

An inexpensive, self-catalysed process is demonstrated for creating a bifunctional electrocatalyst with 3D sea urchin structure. The synergistic improvement in the ORR/OER activities and Zn-air batteries resulting from the combination of CoS_x core, porous carbon shell and Co,N-co-doped CNT are confirmed, indicating a potential candidate for replacing expensive Pt/C and IrO_2 electrocatalysts.

Keywords: Zn-air battery; oxygen electrode; bifunctional electrocatalyst; self-catalysed growth; synergistic effect.

Qian Lu, Jie Yu, Xiaohong Zou, Kaiming Liao,* Peng Tan, Wei Zhou, Meng Ni and Zongping Shao*

Tittle:

Self-Catalysed Growth of Co, N-co-Doped CNTs on Carbon-Encased CoS_x Surface: A Noble-Metal-Free Bifunctional Oxygen Electrocatalyst for Flexible Solid Zn-Air Batteries